Journal of Materials Chemistry C

PAPER

Cite this: J. Mater. Chem. C, 2016, 4, 10852

Formation mechanism of graphene quantum dots and their edge state conversion probed by photoluminescence and Raman spectroscopy†

Gone Rajender[a] and P. K. Giri*[ab]

Received 11th August 2016,
Accepted 21st October 2016

DOI: 10.1039/c6tc03469a

www.rsc.org/MaterialsC

We investigate the formation mechanism of graphene quantum dots (GQDs) from a graphene oxide (GO) precursor and study the inter-conversion of edge states during thermal annealing of GQDs through various microscopic and spectroscopic tools. Monitoring the early stages of growth of GQDs reveals that the in-plane epoxy (C–O–C) functional groups attached at the defect sites essentially cut the oxidized GOs into small pieces of GQDs during the hydrothermal reaction. By conducting a series of controlled annealing experiments under oxygen and hydrogen gas environments, we monitor and quantify the inter-conversion of edge states and functional groups in GQDs from Raman and photoluminescence (PL) studies. The deconvolution of the Raman spectrum allowed us to monitor the evolution of new Raman bands at ~1260 and ~1438 cm^{-1}, which are assigned to the edge functional groups. Through the fitting of the PL spectra and a quantitative analysis of integrated intensities of PL, we unambiguously assign the blue PL emission bands at ~407 and ~440 nm to zigzag and armchair free edge states in GQDs, respectively, for the first time. On the other hand, the green emission bands at ~490 and ~530 nm are attributed to COOH/C–OH and C=O/C–O edge functional groups, respectively. Our conclusions are corroborated by XPS and FTIR spectroscopic analyses of the as-grown and annealed GQDs.

1. Introduction

After the discovery of graphene,[1] graphene-based functional materials, such as graphene oxide (GO) and reduced graphene oxide (rGO), have been intensively studied for both fundamental understanding and practical applications.[2–5] Graphene is a one-atom thick covalently bonded sp^2 carbon prototype 2D material, while GO is known to be the functionalized few layered graphene with functional groups that are attached on the basal plane, and rGO is commonly known to be the more conductive form of GO due to the removal of basal plane functional groups from the sp^2 conjugated carbon network. Graphene quantum dots (GQDs) represent an emerging class of zero-dimensional (0D) materials that show a pronounced quantum confinement effect and plenty of edge states and functional groups.[6–9] It is reported that GQDs of size smaller than ~100 nm possess strong edge effects and quantum confinement.[10] On the other hand, GO and rGO are usually large area graphene sheets and have fewer edge states without exhibiting any edge-state related photoluminescence (PL).[2,3] Interestingly, the edges of GQDs are more reactive than the basal plane because of the high ratio of edge to basal plane carbon atoms.[11] Nevertheless, visualization of such ideal edges is rare due to the requirement of atomic resolution imaging and preparation of ideal samples for direct measurements.[4,5,12–14] However, the presence of abundant edge states and oxygenated functional groups plays a major role in dictating the optoelectronic properties of GQDs and ensuing their application in sensors, bioimaging, energy and environment.[15–18] In addition, owing to their low toxicity, excellent solubility, chemical inertia, stable photoluminescence, and better surface grafting, GQDs are considered to be a promising material for replacing the conventional semiconductor QDs.[17]

A lot of efforts have been made to prepare GQDs through the top down and bottom up approaches. Top down techniques include the cutting of bulk sp^2 bonded carbon materials (such as carbon fibres, graphite, or graphene nanosheets, carbon black, *etc.*) through solvothermal routes,[19] hydrothermal treatment,[20] chemical exfoliation,[21] oxidative cutting,[22] *etc.* On the other hand, bottom-up approaches make use of the self-assembly of organic materials as a precursor, including intermolecular dehydrolysis of citric acid,[23] microwave assisted heating of glucose[24], thermal plasma jet, *etc.*[25,26] Though the top-down approach is more commonly adopted for the preparation of high quality GQDs, the formation mechanism of

[a] Department of Physics, Indian Institute of Technology Guwahati, Guwahati 781039, India. E-mail: giri@iitg.ernet.in; Fax: +91 361 258 2749
[b] Centre for Nanotechnology, Indian Institute of Technology Guwahati, Guwahati 781039, India

† Electronic supplementary information (ESI) available. See DOI: 10.1039/c6tc03469a

GQDs from the cutting of GO is not well understood in the literature. Recent *in situ* study on the atomic structure of GO through aberration corrected TEM revealed nanometer sized crystalline domains in polycrystalline GO films.[5] However, their implication for the formation of GQDs has not been addressed. In some cases, the formation of GQDs was studied on the basis of longitudinal unzipping of carbon nanotubes (CNTs), and the resulting GQDs had irregular shapes.[27] The mechanism of formation of GQDs with nearly circular cross-section from GO has not been addressed properly.

Next, the intriguing mechanism of PL from GQD has been poorly understood. Most of the PL studies on GQDs have been performed in aqueous solution or on GQDs dispersed in a solvent medium, which may have contribution to the resulting PL. Previous studies reveal that the PL emission arises mainly from the size effect, edge sites and oxygenated functional group defects. Generally, the PL mechanism from GQDs is explained on the basis of intrinsic state (blue PL) and defect state emission (green PL). The intrinsic states arise from the size/edge defects where the recombination of electron–hole pairs takes place, while the defect states correspond to the attachment of functional groups.[18,19,22,28–30] To date, very few reports have investigated the exact origin of the broad PL emission from GQDs.[8,31,32] Recently Du *et al.*[33] investigated the effect of functional groups on the PL evolution, and Yoon *et al.*[34] concentrated on the intrinsic state PL emission from GQDs. However, direct monitoring of intrinsic states, defect state evolution and the identification/assignment of edge states in GQD thin films through a combined PL and Raman study is lacking in the literature. Since the solvent contribution can be significant to the PL from GQDs, studies of thin films of GQDs may enable an unambiguous identification of species responsible for specific PL bands. Further, controlling the edge states and functional groups in GQDs is extremely important for their future optoelectronic and biomedical applications. Broad Raman spectra in the range 1000–1815 cm^{-1} have been reported in GQDs by several groups, though the exact origin of the corresponding modes is poorly understood.[29,30,34,35] To the best of our knowledge, Raman deconvolution for intrinsic and functional group defect states in GQDs and their manipulation through controlled annealing has not been addressed in the literature. Non-destructive evaluation of edge states and functional groups in GQDs through PL and Raman studies constitutes an important milestone for their successful application in various emerging areas of science and technology. Thus, the present work focuses on unravelling the formation mechanism of spherical GQDs, and the evolution of the edge states and functional groups during annealing through PL and Raman spectral evolution to gain a better insight into the defect engineering of GQDs.

In this report, we first discuss the formation mechanism of GQDs from oxidized GO (OGO) and rGO sheets with the help of HRTEM, TGA/DTG, and FTIR spectroscopic analyses. Several experimental tools are adopted to understand and probe the in-plane epoxy functional groups in OGO and rGO. Our results reveal that in-plane epoxy functional groups attached at the defect sites play a leading role in the cutting of OGO into GQDs. In comparison to OGO, rGO has less in-plane epoxy functional groups, which limits the formation of GQDs, indicating that the OGO is a better precursor for the synthesis of GQDs. We have provided an improved understanding on the origin of intriguing PL from GQDs, which is currently under intense debate. In particular, we have systematically probed the conversion of edge states in GQD thin films with controlled annealing using PL and Raman analyses. Our results enable unambiguous identification of the zigzag and armchair edges of GQD through PL studies for the first time. In addition, PL emissions corresponding to the COOH/C–OH and C═O/C–O edge oxygenated functional groups were also identified clearly. We have deconvoluted the first order Raman spectra of GQDs in the range 1000–1815 cm^{-1} by Gaussian/Lorentzian peak fitting, and a quantitative correlation between the Raman and PL spectra from GQDs is established for the first time. The Raman spectral band assignments and their significance from Raman spectra are elaborated in detail. Besides the characteristic Raman D, G and D′ bands in graphene, new Raman bands and their evolution with annealing are monitored in GQDs and peak assignments are made based on PL, FTIR and XPS analyses. Detailed analysis of the Raman and PL spectra reveals that the edge states and functional groups in GQDs can be tailored through controlled annealing under a controlled environment.

2. Experimental

2.1. Synthesis of GO and rGO

GO was synthesized by a modified Hummers method, as reported elsewhere.[36] Briefly, 3 g of expandable graphite flakes (EGFs, purity 99%) and 1.5 g of $NaNO_3$ were added to 69 ml of concentrated H_2SO_4 and stirred for 2 h to obtain a uniform solution. Next, the mixture was transferred into an ice bath and 9 g of $KMnO_4$ was subsequently added dropwise under stirring to avoid explosion. The mixture was stirred at 35 °C for 4 h to allow oxidation. Deionized water (DI) was slowly added to the mixture and stirred at 98 °C for 15 min. Further, the solution was diluted with DI water (700 ml) before being quenched with 15 ml of 30% H_2O_2. Additional DI water was added to get the aqueous solution. Subsequently, the final solution was centrifuged at 10 000 rpm for 10 min and the process was repeated for 3 cycles to remove the impurities. Later it was filtered through a 0.22 μm PTFE membrane and dried at 100 °C in an oven to obtain the GO powder. The experimental details of the preparation of rGO are provided in the ESI† (SI-1).

2.2. Size reduction of GO

In order to reduce the size of the GO sheets, the as-synthesised GO sheets were further oxidized with concentrated H_2SO_4 and HNO_3 mixture (volume ratio 1 : 3) with 1 mg of GO. The resulting product is referred to as oxidized GO (OGO).

2.3. Synthesis of GQDs

GQDs were synthesised by a hydrothermal method using OGO as the precursor material. Typically, 50 mg of OGO powder was

mixed with 50 ml of DI water and was sonicated for a few minutes to achieve a uniform dispersion. Next, the mixture was transferred into a Teflon lined autoclave (100 ml) and heated at 200 °C for different reaction durations (12 and 24 h). The reaction temperature was fixed based on the TGA result of OGO, as shown in Fig. S1 (ESI†). The TGA profile suggests the decomposition temperature as ~200 °C for OGO through the loss of in-plane epoxy functional groups. Thus, the knowledge of the decomposition temperature is the key to obtain GQDs through hydrothermal reaction. For the sake of convenience of discussion, 12 and 24 h reaction grown GQD samples are named as S12 and S24, respectively. Experimental details of the synthesis of GQDs using rGO as a precursor are provided in the ESI† (SI-2).

2.4. Functionalization of GQDs

Functionalization of GQDs was carried out *in situ* with the addition of ploy(ethylene glycol) (PEG, average molecular weight 1500) during the GQD synthesis using the above protocol. PEG (3 mg) was added during growth, which was carried out for 12 h and 24 h duration. GQDs functionalized for 12 and 24 h are named as S12F and S24F, respectively.

2.5. Fabrication of GQD thin films

As-synthesized GQDs were re-dispersed in DI water and were sonicated for a few minutes. Prior to the fabrication of GQD thin films, the Si and quartz substrates were cleaned with 2-propanal, acetone and DI water for a few minutes to remove dust and organic impurities. Next, the GQD dispersion was spin coated onto the Si and quartz substrates.

2.6. Hydrogenation and oxygenation of GQD thin films

To understand the mechanism of intriguing PL originating from the edge states and functional groups of GQDs, we conducted thermal annealing of GQDs under different gas environments. Recently, He *et al.* reported a significant finding on the conversion of graphene zigzag edges to armchair and zigzag 57 type edge defects after annealing above 600 °C.[37] To monitor the effect of such conversion on the PL and Raman spectral evolution, we performed annealing at 620 °C under H_2 (purity 99.9%) and O_2 (purity 99.999%) gas environments for 2 hours in each case. The samples were kept in an alumina boat and loaded into a tubular quartz chamber, which was mounted inside a muffle furnace. GQDs spin coated onto the Si and quartz substrates were annealed under identical conditions. Initially, the chamber was pumped down to a base pressure of 5.0×10^{-4} mbar, and the temperature was ramped up to 620 °C at a heating rate of 5 °C min^{-1}. The temperature was maintained at 620 °C and the gas flow rate was maintained at 150 SCCM (standard cubic centimetres per minute) for a duration of 2 h. We believe that the edge sites can be more reactive with a certain gas environment and subsequently attach/detach edge oxygen functional groups depending upon the gas environment, and this leads to functionalization with the edge carbon atoms. It has been reported that the chemical reactivity of edge states in the presence of O_2 gas is about 2000 times higher than that of in-plane carbon atoms in GQDs.[38] To the best of our knowledge, the optical signature of edge state conversion in GQDs is addressed here for the first time. Note that the sample codes used for the hydrogenated and oxygenated samples are represented by the suffix 'H' and 'O', respectively. For example, S12H refers to hydrogenated S12, S12O refers to oxygenated S12, *etc.*

2.7. Characterization techniques

The morphological features and crystalline quality of the GQDs were assessed by high-resolution transmission electron microscopy (HRTEM, JEOL 2100) operated at 200 kV and by selected area electron diffraction (SAED). The type of edge states and crystalline nature of GQD thin films were estimated from Raman spectroscopy using a high resolution spectrometer (Horiba, LabRam HR) with excitation wavelengths of 632.8 nm (He–Ne laser) and 514.5 nm (Ar ion laser). The excitation source was focused with a 100× objective lens and 1 mW laser power was used to avoid laser heating and damage to the sample. The Raman signal was collected by a CCD in a backscattering geometry sent through a multimode fibre grating of 1800 grooves per mm. Edge functional groups and chemical composition of GQDs were analysed from X-ray photoelectron spectroscopy (XPS) measurements (PHI X-Tool, ULVAC-PHI Inc.) using an Al Kα X-ray beam (1486.6 eV) with a beam current of 20 mA. The UV-visible-NIR absorption spectroscopy measurements were performed using a commercial spectrophotometer (Shimadzu, UV3101PC). PL measurements on GQD thin films were carried out at room temperature using a commercial fluorimeter (AB2, Thermo Spectronic) using an external laser (355 nm) excitation source and a suitable filter. Atomic force microscopy (AFM, Agilent, Model 5500) images were recorded in a non-contact operation mode. TGA data were obtained using a STA 449 F3 Jupiter DSC analyser (Netzsch, Germany) equipped with a high temperature tungsten furnace (1700 °C) at a heating rate of 5 °C min^{-1} by purging high purity Ar gas. FTIR measurements were carried out using a commercial spectrometer (Perkin Elmer, Spectrum BX). Some of the powder samples were measured with KBr as a reference.

3. Results and discussion

3.1. Morphological studies

In the process of preparing GQDs from OGO, the structural changes in OGO were monitored by HRTEM analysis as a function of the duration of hydrothermal reaction. The TEM images and the corresponding digital photographs of pristine GO, OGO and rGO are shown in Fig. S2 (ESI†). Fig. S2(a) (ESI†) reveals a large lateral size of the GO sheet. After oxidation with H_2SO_4 and HNO_3, the GO sheets are fragmented to smaller sizes as evident from the TEM image of Fig. S2(b) (ESI†). Fig. S2(c and d) (ESI†) shows the optical photographs of GO dispersion in water and OGO in H_2SO_4 + HNO_3 (oxidation) mixture, respectively. Fig. S2(e) (ESI†) depicts the few layer rGO sheets and the inset shows the SAED pattern indicating the highly crystalline nature of the hexagonal sp^2 carbon sheet. In contrast, the SAED pattern of GO and OGO shows quite a distorted/strained lattice which might be due to the presence of oxygenated functional groups, which is clearly

seen in the case of OGO (see the insets of Fig. S2(a and b), ESI†). Fig. 1(a) shows the TEM image of the S12 sample showing pore formation due to the hydrothermal reaction for 12 h, and Fig. 1(b) shows a magnified view of the image (a). During the hydrothermal reaction, in order to release the strain in the OGO lattice, the epoxy functional groups may form a closed/quasi-ring type structure on the basal plane of OGO.[39] It is apparent from Fig. 1(a and b) that pore formation occurs in OGO during the hydrothermal reaction under high temperature and high pressure. The average diameter of the pores is ~16 nm (see Fig. 1(b)). This implies initiation of the cutting of OGO sheets through which the strain might be released and we believe that the epoxy pairs attached at the defective sites of GO may have a very important role in the cutting of the OGO sheets. One may also argue that the holes in OGO could form by oxidative widening of existing defects through attack on the internal edges of the OGO and the epoxy ring like structure may not be essential for the cutting of the OGO sheets. In order to lend support for the necessity of the epoxy functional groups, we studied the effect of hydrothermal reaction on the rGO sheet. Interestingly, it was found that for hydrothermal reaction with rGO under similar conditions (12 h reaction), no distinct GQDs were formed (see Fig. S2(f), ESI†). Despite the strong presence of structural defects in rGO, oxidative cutting of rGO does not take place during hydrothermal reaction. This establishes the critical role of epoxy functional groups on the basal plane of OGO in the cutting of the OGO sheets to form GQDs. However, high-resolution TEM including aberration-corrected TEM studies would be helpful to gain better insight into the actual structure of these pores.[4,5] It may be noted that atomic scale imaging of GO and rGO has been reported in the literature,[4,5] while very little information is available on the actual structure of GQDs.[6] Fig. 1(c) represents a TEM image of GQDs at a different location of S12, which shows small GQD fragments that are separated from the OGO sheet after the hydrothermal reaction. The reaction for longer duration (24 h) yields smaller sized GQDs, as shown by the TEM image of the S24 sample (see Fig. 1(d)). The inset of Fig. 1(d) shows the SAED pattern of GQDs and it signifies the presence of few layer graphene in GQDs. The average size of GQDs is ~5 nm for the S24 sample. These results are in good agreement with the spectroscopic and TGA/DTG results (discussed later).

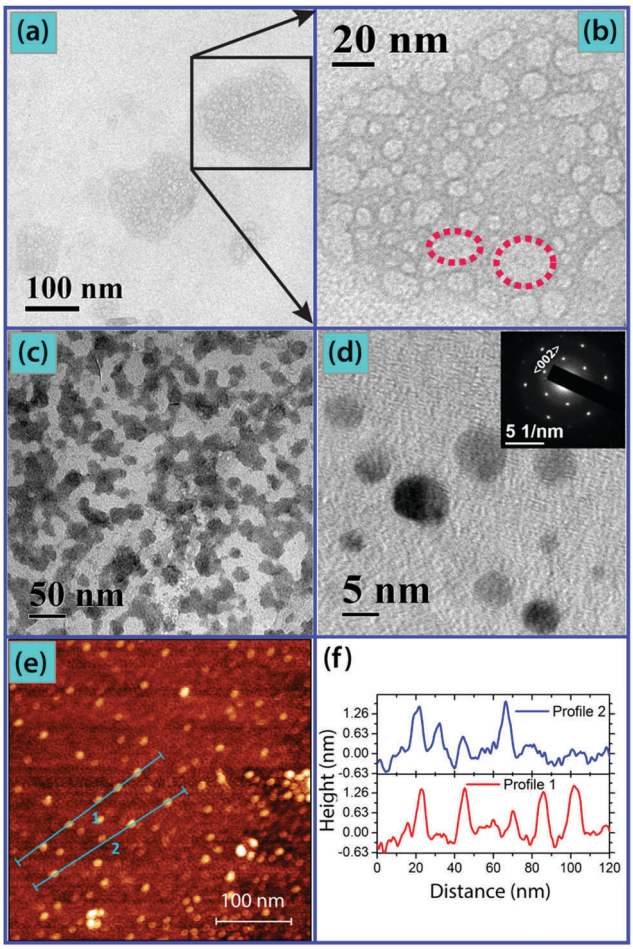

Fig. 1 (a) A TEM image of the early stage of growth of GQDs with pore structures in S12, and (b) a magnified view of a portion of the image in (a). Dotted circles in (b) represent the oxygen functional group ring formation on the basal plane of the OGO sheet. (c and d) TEM images of GQDs in S12 and S24 samples, respectively. The inset of (d) shows the SAED pattern indicating the hexagonal structure and it is significant for the few layered GQDs. (e) AFM image of GQDs in S24, and (f) AFM height profile of GQDs measured along the line 1 and 2 shown in (e).

Fig. 1(e) represents the AFM image of GQDs in the S24 sample and the solid lines are drawn to obtain the height profile of the GQD layers, as shown in Fig. 1(f). The AFM image of GQDs and the height profile of the GQD layers further confirm that the GQDs consist of a few (1–5) layers of graphene, consistent with the SAED pattern. Note that during the formation of GQDs, first the porous GO is formed, where the pore size can be controlled by the reaction condition. The porous GO is an interesting material for gas molecule adsorption, energy storage devices, nano-electronics, catalysis and supercapacitor applications.[40–42] Thus, we emphasize that the present synthesis process leads to the production of size controlled GQDs as well as porous GO sheets that are suitable for various emerging applications.

3.2. Formation mechanism of GQDs

Note that the as-prepared GO has various functional groups on the basal plane and at the edges. The intrinsic atomic structure of defective GO has been recently reported by Dave *et al.*,[5] which revealed that nanocrystalline regions (size ~2–4 nm) of the sp^2 lattice in GO are surrounded by regions of disorder, where the in-plane functional groups are attached. Generally the epoxide and hydroxyl groups are attached on the basal plane of GO and the carboxylic (COOH), carbonyl (C═O), lactone, pyrone, ether and other functional groups are decorated at the edge sites.[43–45] An epoxide is cyclic ether with a three-atom ring. This ring approximates to an equilateral triangle, which makes it highly strained. The strained ring makes epoxides more reactive than other ethers. It is reported that epoxy functional groups are very reactive sites and can easily modify the GO structure through ring-opening reactions.[46] Li *et al.*[27] reported that the strain generated by the cooperative alignment of epoxy groups can initiate fault lines and create cracks on GO. Further, the continuation

of unzipping processes can be identified by binding of a new epoxy group during the oxidation or hopping of an existing epoxy group and subsequent locking. With the help of simulation and experimental results, previous studies have established that in-plane epoxy functional groups are very important and once an epoxy chain appears, it is energetically favourable for it to be further oxidized into epoxy pairs that then convert to more stable carbonyl pairs at room temperature.[47–49] Note that the reported models and experimental results have mostly discussed about the unzipping of CNTs and cutting of GO that takes place along the C–C line. However, this type of cutting results in the growth of a 1-D structure (*e.g.*, graphene nanoribbons) or a particular type of oriented structure of carbon (zigzag or armchair).

Note that a good understanding of the mechanism of formation of circular shaped GQDs remains elusive. In the present case, the epoxy functional groups attached at the defect sites are believed to form a co-operative quasi-ring type closed structure along the C–C bond to yield nearly circular shaped GQDs by the cutting of OGO, as confirmed with the HRTEM analysis. Analyses of the FTIR and UV-Vis absorption data (see Fig. S3 (a and b), ESI†) of OGO strongly suggest the presence of in-plane epoxy functional groups on the basal plane of OGO, while they are absent in rGO. The vibrational mode at 1384 cm^{-1} in OGO is due to the epoxy deformation,[21] the broad peak in the region 3100–3600 cm^{-1} is due to the attachment of hydroxyl groups and two other modes at 1580 and 1650 cm^{-1} are attributed to the in-plane stretching vibrations of sp^2 bonded carbon atoms and COOH functional groups, respectively (see Fig. S3, ESI†).[50] The UV-Vis absorption spectrum of OGO shows a broad absorption band extending from the UV to the entire visible region, indicating that in-plane functional groups cover the basal plane of OGO, while in rGO the intensity is reduced, presumably due to the low density of functional groups. In addition, the TGA profile of OGO (see Fig. S1, ESI†) further supports the assertion regarding the decomposition of OGO due to the loss of in-plane epoxy functional groups.[45] Similarly, the TGA/DTG result of rGO showed very low weight loss (%) at 200 °C as compared to that for OGO, most probably due to the lack of in-plane oxygen functionalities. In addition, rGO showed additional DTG peaks at 230, 307, 436, and 812 °C, which are believed to be due to the residual epoxy/C–O (ether), COOH and C═O functional groups and sp^2 hybridized carbon. TEM imaging results of GQDs synthesised using two different precursor materials further support the distinct role of in-plane epoxy functional groups in the formation of high quality GQDs. Fig. 2 shows a schematic representation of the proposed formation mechanism of GQDs from the cutting of OGO sheets with the help of epoxy rings. Note that the degree of oxidation of GO, solvent, and reaction temperature will have a strong influence on the structure and morphology of GQDs. In the first step, the epoxy functional groups in OGO tend to appear at the C–C bond and form a quasi-ring type structure underlying the C–C bonds on the basal plane of OGO (see Fig. 2(a)). Formation of quasi-ring type epoxy functional groups and porous structure of OGO is evidenced from the TEM imaging results (see Fig. 1(b)). In the second step, once the epoxy pairs form they are energetically favourable to cut the OGO into small pieces, as shown in Fig. 2(c), and finally small sized GQDs are formed (Fig. 2(d)). Note that this cutting need not be mediated by the defects or hydroxyls.[45,48,49] Further, the GQD fragments that are separated from OGO sheets have a size similar to that of the pore size, indicating that the GQDs are indeed formed due to the cutting of the OGO sheets (see Fig. 1(c)). A reaction duration of 24 h results in smaller size fragments and formation of smaller sized GQDs ($\sim$5 nm, see Fig. 1(d)). The proposed mechanism is fully consistent with the formation of nearly circular shaped GQDs with different edge states, oxygen functionalized and defective GQDs. Interestingly, the measured size of GQDs is quite consistent with the recent finding of the 2–4 nm nanocrystalline region in GO, as revealed from aberration-corrected TEM imaging.[5] Recently, Alam *et al.*[51] proposed a model through DFT calculations and showed that the selective cutting of graphene sheets into edge states led to the formation of size controlled GQDs. We believe that our experimental results provide a better understanding of the formation mechanism of GQDs. The growth mechanism discussed above is believed to be consistent with other preparation methods. However, more studies on simulation, *in situ* experiments and atomic resolution imaging would be required to clarify the precise mechanism behind the formation of circular cross-section GQDs.

3.3. Raman study of the GQD edges and functional groups

Fig. 3 shows a comparison of the Raman spectra of S12F and S24 before and after annealing. The as-grown samples show multiple Raman bands, some of which are characteristic modes of graphite, such as D, G and D′ bands. After annealing, the peaks are broadened and the relative intensity of the D band is enhanced as compared to that of the G band. The characteristic G band is due to the in-plane vibrations of sp^2 carbon (E_{2g} mode), while the D′ band is attributed to the vacancies and/or pentagonal and octagonal defects, usually referred to as zigzag 5–7 defects.[52–54] In order to gain a better insight into the edge states and functional group defects in GQDs, the broad Raman spectrum in the range 1000–1815 cm^{-1} was deconvoluted. The deconvolution of the Raman spectrum is essential for understanding the disordered graphitic materials.[55] Sadezky *et al.*[54] described a five peak model for the fitting of the Raman spectra of carbon soot and related carbonaceous materials, and Claramunt *et al.*[53] proposed a five peak model for the fitting of Raman data of GO. Similarly, Rebelo *et al.*[56] recently proposed a multi-peak Raman fitting for multiwalled CNTs and studied the covalent functionalization by diazonium chemistry and oxidation methodologies. In the present case, we find that six peaks were necessary to fit the broad Raman spectra of GQDs. Note that besides the well known D, G and D′ Raman modes, new Raman modes D1, D2 and D3 are fitted to the experimental data (Fig. 3). D1, D2 and D3 are well fitted with Gaussian peaks, while the characteristic D, G and D′ bands are fitted with Lorentzian peaks. Generally, some of the Raman-inactive modes become active due to the presence of structural defects that are created during the cutting (growth) and/or attachment of various functional groups in GQDs. The edge is a special kind of disorder and the nature of edges can be

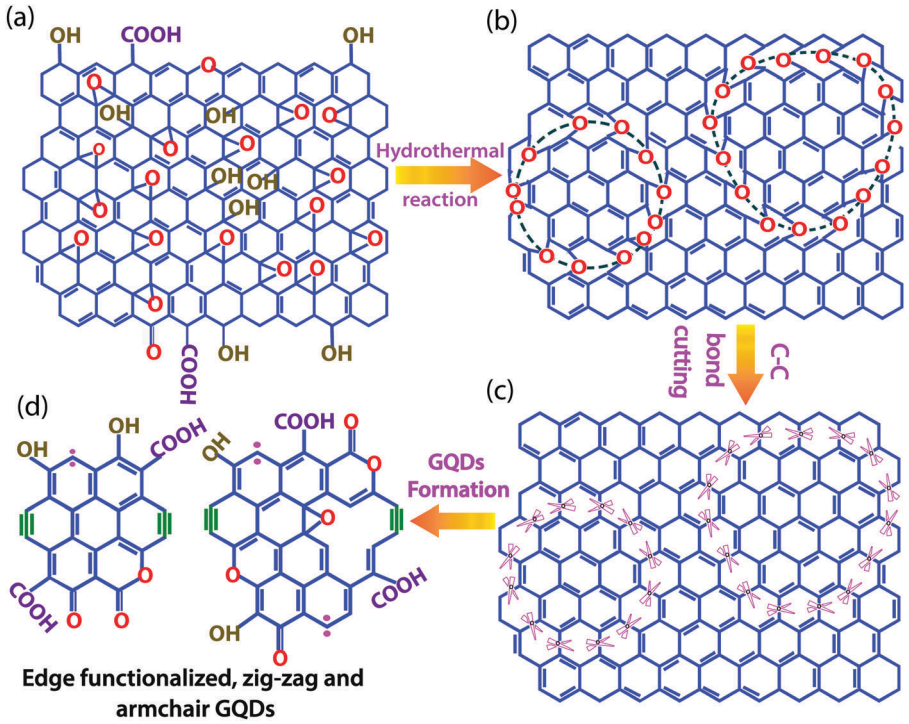

Fig. 2 A schematic illustration of the proposed formation mechanism of GQDs from OGO sheets. (a) Schematic representation of the in-plane epoxy (C–O–C) and OH functional groups on the OGO sheet, and (b) the dashed circle with oxygen atoms represents the epoxy quasi-ring formation underlying the C–C bonds during the hydrothermal reaction. (c) Cutting process of the C–C bonds in the OGO sheet. (d) Formation of circular/quasi-circular GQDs through the cutting. Separated GQDs possess zigzag and armchair edges and functional groups. Magenta dots and olive colour bonds refer to the zigzag and armchair sites, respectively.

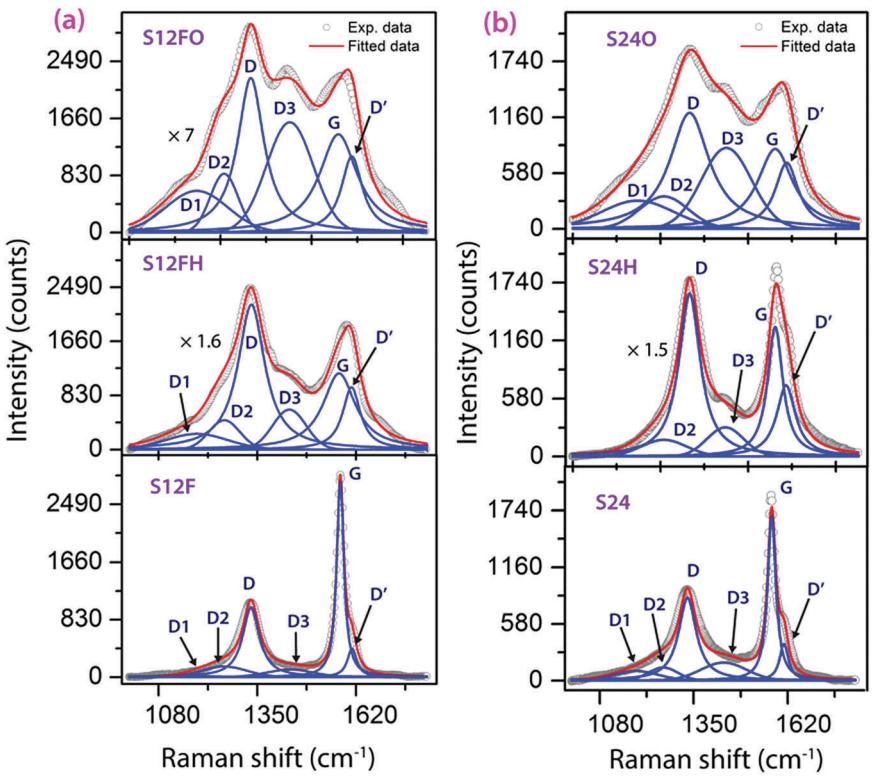

Fig. 3 Raman spectra of various GQD thin films fitted with Lorentzian and Gaussian peaks. (a) S12F, S12FH and S12FO samples, and (b) S24, S24H and S24O samples. To enable comparison of intensity, some of the spectra are magnified with appropriate factors, as mentioned in each case. Note that 632.8 nm laser excitation is used for Raman measurements. The experimental data are shown with symbols and the fitted data are shown with a red line. The new Raman bands D1, D2, and D3 correspond to the sp^2–sp^3 carbon, COOH/C–OH and C=O/C–O edge functional groups, respectively.

probed by the intensity of the Raman D band. The D band arises from the momentum conservation law due to the formation of edge states (zigzag and armchair). It has been reported that the intensity of the Raman D band is very sensitive to the nature of edge states in GQDs. It is strongly present for the armchair edges and nearly absent for the zigzag edges.[57–61] The additional bands D1, D2, and D3 may be related to functional group defects. The parameters of the fitted peaks are presented in Table T1 (ESI†). The ratio of intensity of the D to G band (I_D/I_G) is 0.83 for the S12F sample. Interestingly, after annealing, the I_D/I_G ratio is nearly doubled for the S12FH sample and it is increased to 1.08 for the S12FO sample. Since the D band intensity is most sensitive to the armchair edge states, the increased D band intensity (ratio) after annealing clearly reveals the conversion of the edges from zigzag to arm chair type. The low intensity of the D band in S12F indicates the presence of both types of edges, zigzag and armchair, while the increased D band intensity in S12FH and S12FO suggests the dominance of armchair edges due to the conversion from zigzag to armchair sites after annealing. A similar trend in change in intensity ratios is observed for S12, S12H and S12O samples and the results are shown in Fig. S4 and Table T1 (ESI†). For S24, the I_D/I_G ratio is 1.07, while after annealing the ratio is increased to 1.75 and 1.62 for S24H and S24O, respectively (see Table T1, ESI†). These results strongly suggest that the zigzag edges of GQDs are converted to armchair edges and the annealed samples contain primarily the armchair edges. This result is consistent with the quantitative analysis of PL data, discussed later.

Next, we address the evolution of the edge oxygenated functional groups in GQDs after annealing. It is noted that the edge carbon atoms are reconstructed during annealing and the sp^2–sp^3 bonding changes in order to maintain the stability of edge carbon atoms.[12,52] In S12, the I_{D1}/I_G ratio is increased by five-fold after H_2 annealing and by about ten-fold after O_2 annealing. A similar increase in the intensity ratio is observed for S12F and S24 (see Table T1, ESI†). Thus, the D1 band at $\sim$1185 cm^{-1} may be attributed to the sp^2–sp^3 bonded carbon atoms at the edges of GQDs. In the same way, we monitored the I_{D2}/I_G ratio for different GQD samples before and after annealing. The ratio I_{D2}/I_G is marginally higher after both oxygen and hydrogen annealing. Since the thermal stability of C–OH functional groups is higher than that of C═O groups,[62] the D2 band may be attributed to COOH/C–OH functional groups. This is in accordance with the FTIR and XPS analyses. In the case of H_2 annealing, C–H bonds may be present at the GQD edges.[63] Thus, the increase in the I_{D2}/I_G value after H_2 annealing is expected due to the formation of C–H bonds or due to the residual C–OH functional group. A similar trend is observed in other samples (see Table T1, ESI†). For the band D3 centred at $\sim$1438 cm^{-1}, the intensity ratio I_{D3}/I_G is remarkably increased after annealing in O_2 due to the formation of covalent bonds between the oxygen and the edge carbon atoms, *i.e.*, C═O/C–O bonds at the GQD edges. The I_{D3}/I_G ratio is only 0.16 for the S12F sample, while it is 5.5-fold increased in the S12FO sample after O_2 annealing. For S24, the I_{D3}/I_G ratio is increased from 0.39 to 0.95 after O_2 annealing (see Table T1, ESI†). These results strongly suggest that oxygen functionalization takes place at the GQD edge sites, which can be easily controlled through post growth annealing. On the other hand, H_2 gas annealing causes a relatively small change in the I_{D3}/I_G ratio. The I_{D3}/I_G ratio changed from 0.16 to 0.27 for S12F and from 0.39 to 0.35 for S24 after H_2 annealing. It is reported that C═O functional groups are thermally more stable than the COOH groups.[62] This might be the reason for the observation of the residual C═O functional group after annealing. The increased I_{D1}/I_G ratio after oxygen annealing is attributed to the increased density of sp^2–sp^3 bonds due to the covalent attachment of oxygen atoms at the sp^3 carbon sites. Finally, the D′ band intensity is compared for GQD thin films before and after annealing. The $I_{D'}/I_G$ ratio for the S12F sample is 0.19, while it is 2-fold increased for the annealed samples (S12FH and S12FO). The $I_{D'}/I_G$ ratio for the S24 sample is 0.23, while it is $\sim$3-fold increased for the S24H sample and 2.3 fold increased for the S24O sample. The marginally lower $I_{D'}/I_G$ ratio in the oxygen annealed sample may be due to the fact that some of the oxygen atoms get attached at the defect sites during oxygen annealing. The high temperature (620 °C) annealing may have resulted in the formation of vacancy and pentagon/heptagon (edge reconstruction) defects due to the loss of loosely bonded functional groups (ether) and the conversion of edge states. Note that the stability of ether and lactone type functional groups is relatively low compared to other functional groups.[46] Recent reports suggest that high temperature (600 °C) heating causes formation of pentagon/heptagon defects and reconstructed zigzag (5–7) defects in graphene.[12,37] These results suggest that higher density of defects may be present in GQD thin films after annealing. Thus, the increased $I_{D'}/I_G$ ratio in annealed samples directly implies the formation of additional defects, such as vacancies, pentagon/heptagon defects and reconstructed zigzag (5–7) defects, in GQD thin films. A similar trend is observed in other GQD samples after annealing. Note that besides the removal of functional groups, hydrogenation may allow formation of hydrogen bonds and doping.[63] Additional Raman measurements with 514.5 nm laser excitation showed spectra similar to that obtained with 632.8 nm laser excitation, except some changes in the position of D and D′ bands (see Fig. S6, ESI†). This is due to the dispersion of the D band with different excitation wavelengths.[64]

In a previous study, we assigned the additional Raman band at $\sim$1440 cm^{-1} to the COOH or C═O functional groups.[50] In the present case, our controlled annealing studies reveal that the additional band arises from the covalent attachment of oxygen (C═O/C–O) at edge sites. Dippel *et al.*[65] and Sadezky *et al.*[54] observed a Raman peak at 1190 cm^{-1} in flame soot and attributed it to the sp^2–sp^3 bonds or C–C and C═C stretching vibrations of polyene-like structures. Claramunt *et al.* attributed the Raman band at $\sim$1187 cm^{-1} to oxygen content in GO.[53] Thus, there is controversy regarding the origin of the additional Raman bands near the D band. GQDs are a few nanometer sized sp^2–sp^3 bonded carbon atoms with plenty of edge defects. Due to the cleavage of OGO, the carbon atoms are rearranged and the attachment of oxygen functional groups takes place at the sp^2–sp^3 edge carbon sites. Indeed, the edge carbon atoms are more favourable

for the formation of the sp^2–sp^3 bonds due to the attachment of oxygen functional groups/defects.[52] Thus, the Raman D1 band at ~1185 cm^{-1} is assigned to the sp^2–sp^3 bonded carbon atoms at the edges of the GQDs. The Raman D2 band at ~1260 cm^{-1} is assigned to COOH or ring type C–OH edge functional groups, while the D3 band at ~1438 cm^{-1} is attributed to the C═O/C–O functional groups. Note that the peak assignments are consistent with the evolution of XPS, FTIR and PL spectra from GQDs. Since several theoretical[66,67] and microscopic studies[6,8,22,29] confirm the presence of edge defects in GQDs, our Raman analysis proves to be a powerful tool to monitor these defects more conveniently.

3.4. UV-Vis absorption studies

Fig. 4 shows the UV-visible absorption spectra of different GQD samples. All the samples show the characteristic π–π* transition peak at ~276 nm, which signifies the transition of sp^2 carbon atoms. The other absorption band at ~333 nm is relatively broad and it changes after PEG functionalization, along with the reduction of intensity of the ~276 nm peak. The ~333 nm peak is referred to as n–π* transition and it is mainly due to the attachment of oxygen functional groups (C═O/COOH) at the GQD edges.[23,50] Interestingly, the S24 sample shows a distinct absorption peak at ~276 nm, revealing the ultrafine size of GQDs in the as-grown samples and it arises from the quantum confinement effect. Note that this feature is not prominent in other samples perhaps due to the larger size of the GQDs. This is strongly supported by HRTEM results that show a size of ~5 nm for the S24 sample. Besides the size, the attachment of edge oxygenated functional groups is also evident from the absorption spectra. The absorption band corresponding to the oxygenated functional groups becomes broad after PEG functionalization. It is noted that PEG is a polymer that contains branched COOH functional groups. During the reaction, the COOH functional groups get attached at the GQD edges resulting in the broad absorption band for the functionalized GQD samples.

3.5. Photoluminescence studies

Fig. 5 shows the room temperature PL spectra excited with a 355 nm laser for various GQD thin films before and after annealing.

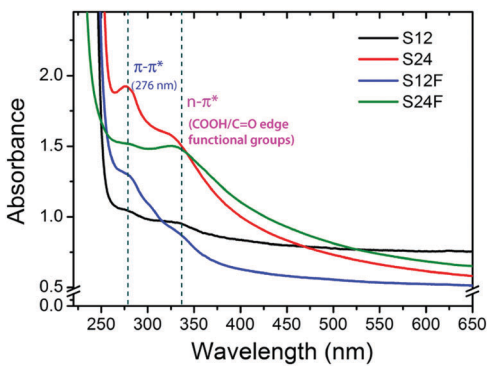

Fig. 4 Comparison of the UV-Vis absorption spectra of different GQDs before and after functionalization with PEG. The π–π* band originates from the band to band (π–π*) transition of sp^2 carbon and the n–π* absorption band corresponds to the sub-band states arising from the COOH/C═O edge functional groups.

Fig. 5(a) shows the normalized PL spectra and Gaussian peak fitting for S12F, S12FH and S12FO, while Fig. 5(b) shows the same for S24, S24H and S24O. All the samples clearly show PL emission in the blue and green regions. It is clear from the asymmetry and shift in the PL spectra (after annealing) that multiple peaks contribute to the strong PL emission from the GQD thin films. A clear understanding of the various PL peaks is achieved by the Gaussian peak fitting of each spectrum. Note that each PL spectrum is fitted with four Gaussian peaks (P1, P2, P3, P4) and different samples show different intensities of these peaks based on the growth and annealing conditions. Typically, the blue and green emissions from GQDs have been assigned to edge defects and functional groups of GQDs.[19,32] However, the nature of edge states has not been distinguished properly through PL analysis and it was found necessary to monitor the evolution of different PL peaks after functionalization and annealing to identify the exact origin of each peak. Interestingly, we found an intriguing correlation between the evolution of the PL peaks with annealing and the new Raman bands discussed in the previous section. Note that there is a drastic change in the relative intensities of peaks P1 (at ~407 nm) and P2 (at ~440 nm) after annealing in both H_2 and O_2 environments. The relative intensity of peak P1 is reduced significantly after annealing, while that of peak P2 is strongly increased after annealing, and there is a one to one correspondence between the intensities of the two peaks. Recently, He *et al.* reported that in graphene nanoribbons the zigzag edges are converted to armchair sites after annealing,[37] and recent simulation results support the edge state stability.[68] Song *et al.* suggested that at high temperatures the armchair edge is the most prevalent edge structure among various edge configurations in graphene.[69] It is noteworthy that based on the report of He *et al.* we have chosen the annealing temperature of 620 °C in order to reduce the zigzag edges and increase the armchair edges in GQDs through the inter-conversion of edges and monitor the corresponding PL evolution. Thus, the drastic reduction in the intensity of peak P1 and the concomitant increase in the intensity of peak P2 after annealing clearly signify the conversion of edge states from zigzag to armchair states and it allows us to unambiguously distinguish the PL peaks related to zigzag and armchair states.

In order to quantify the relative changes in the density of edge states and functional groups with annealing, we monitored the changes in the integrated intensity of the PL peak with annealing. The parameters extracted from the Gaussian peak fitting of the PL spectra are presented in Table 1. Note that all the PL measurements on GQD thin films were conducted under identical conditions to enable comparison. Importantly, we monitor the conversion of edge types due to the thermal annealing, while the edge functional groups are controlled by the annealing environment (H_2 and O_2). Note that the integrated intensity of peak P1 is drastically reduced and that of peak P2 is dramatically increased after H_2 and O_2 gas annealing, and most interestingly this trend is consistently followed in all samples, as shown in Fig. 6(a) and 6(b). The decrease in the intensity of P1 and the concomitant increase in the intensity of P2 follow a trend similar to that of the changes in the Raman D bands of GQDs. Since the annealing

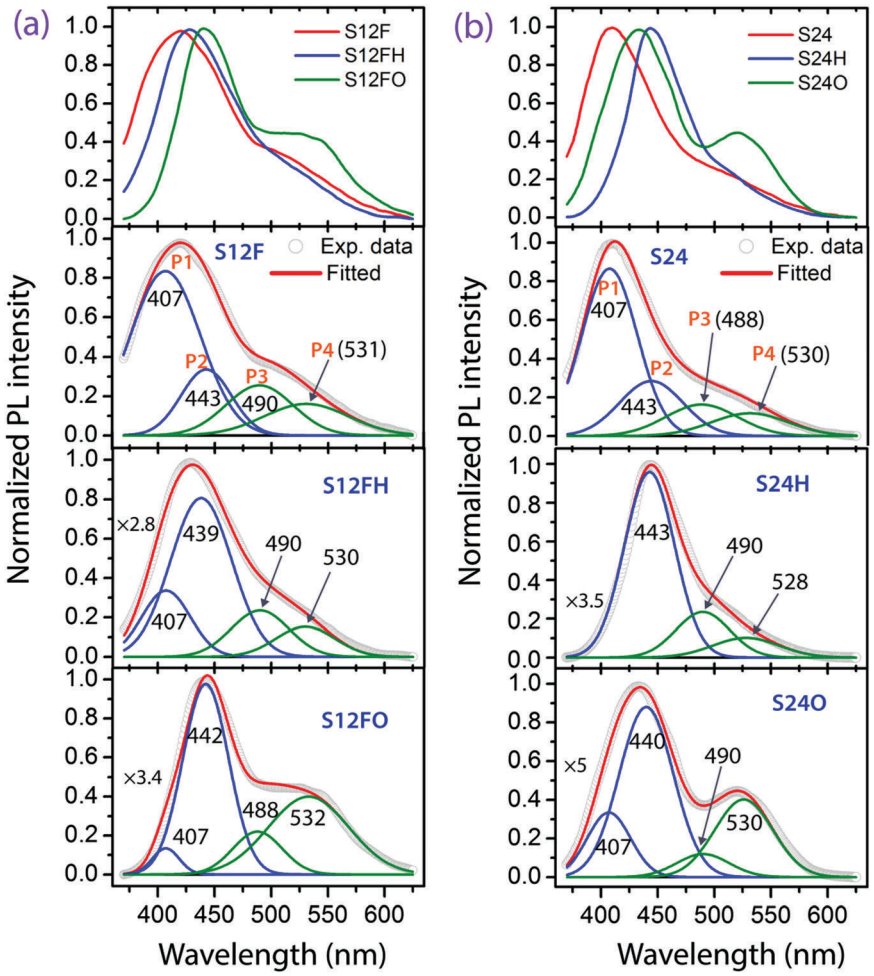

Fig. 5 Normalized PL spectra (excited with a 355 nm laser) at room temperature for various GQD thin films before and after (H_2 and O_2) annealing. (a) Comparison of the PL spectra and the Gaussian peak fitting for S12F, S12FH and S12FO. (b) Comparison of the PL spectra and Gaussian peak fitting for S24, S24H and S24O. Note that peaks P1 and P2 are significant for the zigzag and armchair edge states, while peaks P3 and P4 are significant for the COOH/C–OH and C═O/C–O edge functional groups, respectively. All the peak positions are in nm units. The experimental data are shown with symbols and the fitted data are shown with a red line in each case.

Table 1 Summary of fitted PL peaks (P1, P2, P3 and P4) and their identity for various GQD thin films before and after annealing. The relative percentage of each species is calculated from the integrated intensity of respective peaks for each sample

	Peak position in nm				Relative percentage of edge states and functional groups			
Sample name	P1	P2	P3	P4	Zigzag states	Armchair states	COOH/C–OH	C═O/C–O
S12	407	443	490	529	53	22	12	13
S12H	—	440	490	530	0	72	17	11
S12O	—	440	490	531	0	69	8	23
S12F	407	443	490	531	55	16	16	13
S12FH	407	438	490	530	19	56	15	10
S12FO	407	442	488	533	4	49	12	35
S24	407	443	488	530	55	20	14	11
S24H	—	443	490	528	0	71	19	10
S24O	407	440	490	530	16	52	6	26
S24F	407	440	490	530	44	27	19	10
S24FH	407	443	490	530	11	66	16	7
S24FO	407	440	490	530	17	48	12	23
Peak identity	Zigzag edge states	Armchair edge states	COOH/C–OH	C═O/C–O				

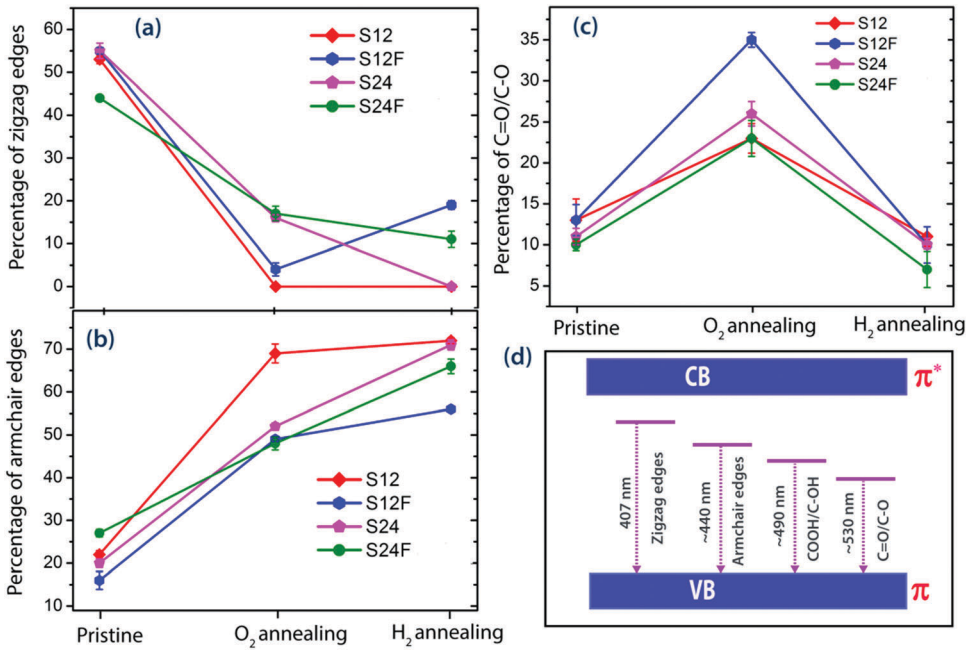

Fig. 6 Quantitative analysis of edge states (zigzag and armchair) and oxygenated functional groups before and after annealing as derived from the relative integrated intensities of PL. Percentage of (a) zigzag edges, (b) armchair edges, and (c) C═O/C–O edge functional groups before and after annealing. (d) Schematic representation of the band diagram of GQDs showing the edge state and functional group related transitions giving rise to two blue and two green PL emission bands.

at 620 °C is expected to convert zigzag edges to armchair edges, the decrease in the intensity of P1 is due to the decrease in the density/percentage of zigzag edges. Similarly, the strong increase in the intensity of P2 after annealing implies the enrichment of armchair edges in GQDs. Thus, peaks P1 and P2 at ~407 nm and ~440 nm, respectively, are assigned to the zigzag (carbene-like, with a triplet ground state being most common) and free armchair sites (carbyne-like, with a singlet ground state being most common) in GQDs. At the same time, during annealing the density of oxygen functional groups is altered, based on the annealing environment. Fig. 6(c) clearly shows that the concentration of C═O/C–O bonds is increased after O_2 annealing, as expected, and it again decreases upon H_2 annealing at 620 °C. Based on the literature report and our annealing results, the two green emission bands P3 and P4 are attributed to the COOH/C–OH and C═O functional groups, respectively.[28,50] This is consistent with the FTIR analysis presented later. Note that the overall PL intensity is reduced in annealed samples which might be due to the creation of additional defects, *e.g.*, vacancies, pentagon/heptagon defects, and some of these defects may act as non-radiative recombination centers. These results are consistent with the Raman analysis that showed the increased $I_{D'}/I_G$ ratio in the annealed samples. We find from the PL analysis that the as-grown S12 sample contains mostly zigzag edges, as evident from Table 1, while the annealed samples (S12H and S12O) contain mostly the armchair edges without any significant presence of zigzag states (see Fig. S5(a), ESI†). The slight increase in the intensity of P3 may be due to the C–H bond formation. Fig. 6(d) shows a schematic representation of the band diagram of GQDs depicting the edge state and functional group related transitions giving rise to two blue (P1, P2) and two green (P3, P4) PL emission bands. Radovic *et al.* proposed a structural model for graphene edges and explained that free zigzag sites are carbene-like with a triplet ground state being most common, while the free armchair sites are carbyne-like with a singlet ground state.[7] Thus, the unambiguous identification and control of graphene edges have been made possible in this study through a careful design of the growth strategy and post-growth annealing.

3.6. XPS studies

In order to gain further insight into the identity of functional groups, XPS analysis was carried out on the GQD samples. Fig. 7 represents the XPS core level C1s and O1s spectra of the S24 sample before and after annealing. Fig. 7(a–c) shows the C1 spectrum of S24, S24H and S24O samples, respectively. Each of the C1s spectra is fitted with five Gaussian peaks to extract the peak parameters properly and the fitted parameters are listed in Table T2 (ESI†). The peaks centered at 284.5, 286.14, 287.5, 290.0, and 293.7 eV are the characteristic peaks assigned to sp^2 bonded carbon (C═C), C–O (ether), carbonyl (C═O), carboxylic (COOH) and shake up satellite peak (π–π*), respectively, and these are consistent with the literature.[19,22,33] It is evident from Table T2 (ESI†) that the relative percentages of C═C, C–O (ether), C═O and COOH in the S24 sample are 39, 22, 13 and 16%, respectively. Interestingly, after annealing the percentage of edge functional groups in S24H and S24O is drastically changed with respect to that of S24. It implies that the functional groups in GQDs can be carefully tuned and monitored by H_2 and O_2 gas annealing, which leads to a significant change in the green PL emission (P3, P4) mentioned earlier. Further, we observed an

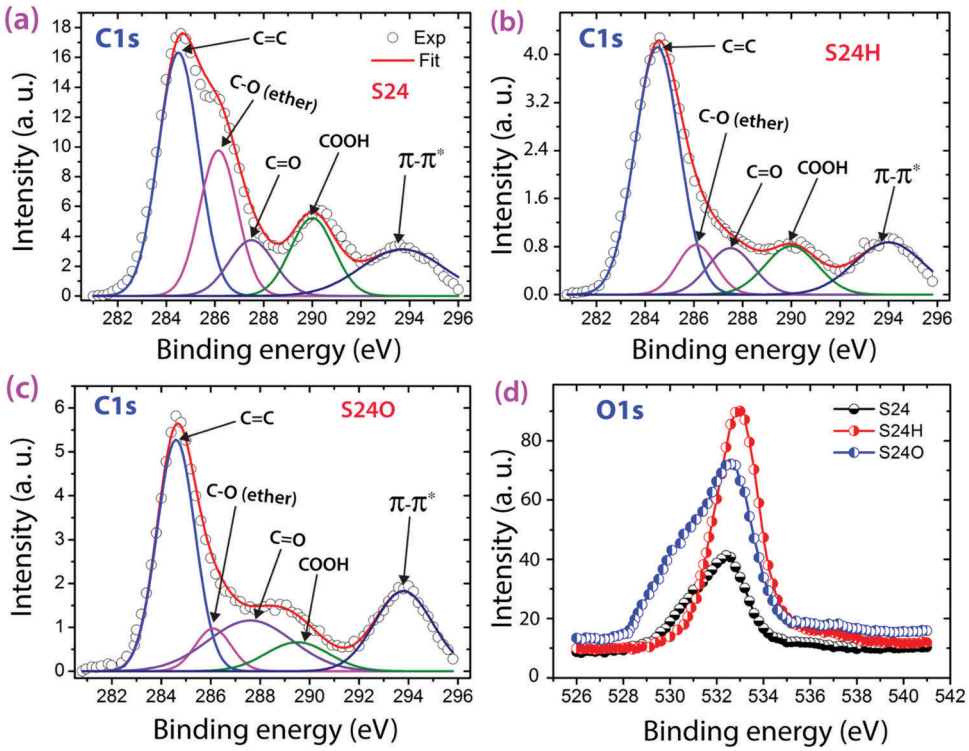

Fig. 7 Core level XPS spectra for various GQD thin films. (a–c) C1s spectra with Gaussian peak fitting for S24, S24H, and S24O samples, respectively. (d) Comparison of the O1s spectra for the S24 sample before and after O_2 and H_2 annealing.

increased concentration of C=C bonds in S24H, as expected. Since some of the edge functional groups are destroyed during the annealing, it results in the relative enhancement of C=C bonds. This is in good agreement with the FTIR analysis (discussed later). Similarly, there is a substantial change in the percentage of the C–O (ether) group in S24H and S24O as compared to that of S24. Note that the as-grown GQDs contain edge defects, ether and edge functional groups (Fig. 2). The atomic percentage of the C–O (ether) group in S24 is 22%, while it reduces by more than half to 9% and 7% for S24H and S24O, respectively. It is to be noted that the ether functional group has lower thermal stability as compared to the other functional groups.[46] In the present case, the high temperature (620 °C) annealing results in the loss of oxygen atoms from the ether group and the vacancy defects are formed and/or edges are reconstructed to form heptagon and pentagon defects, the so called stone-wall (S-W) defects.[12,37] Thus, the formation of vacancy and/or heptagon and pentagon defects is more favorable in the annealed samples. This result is in very good agreement with the Raman analysis that showed an increased intensity ratio of $I_{D'}/I_G$ after annealing (see Fig. 3 and Table T1, ESI†). During annealing, besides the creation of crystalline defects, the conversion of edge states is very efficient in GQDs, as evident from the earlier discussion. Note that the percentage of the C=O functional group in the S24 sample is 10%, while it is doubled in S24O due to O_2 annealing. However, the atomic percentage of the C=O functional group in the S24H sample does not show any substantial change, which might be due to the higher stability of C=O groups.[62] Note that H_2 (purity 99.9%) annealing may also cause partial removal of oxygen functional groups. Besides the C1s spectrum, the O1s XPS spectrum of GQD samples further augmented the increased concentration of oxygen functional groups after O_2 annealing. Fig. 7(d) shows the comparison of O1s spectra for S24 before and after annealing. The integrated intensity of the O1s spectrum for the S24O sample is 1.78 times higher than that of the pristine sample, which reveals the attachment of oxygen atoms at the edge/in-plane sites of GQDs. This is consistent with the enhanced intensity of green PL (530 nm) and the enhanced intensity of the FTIR band related to the oxygenated functional groups after O_2 annealing. Note that the integrated intensity of the O1s spectrum for the S24H sample is 1.56 times higher than that of pristine samples. This might be due to the impurity content in the H_2 gas, adsorbed moisture and residual (C=O) functional groups that strongly bind to the GQD edge sites before the measurement. This is consistent with the considerable green PL (peak P3) emission after the hydrogenation.

3.7. FTIR studies

Fig. 8 shows the characteristic FTIR spectra of GQD thin films before and after H_2 and O_2 annealing. It is evident from the spectra that a substantial change in the intensity of various functional groups occurs after the annealing. All the samples show the characteristic IR active vibrational bands of sp^2 carbon and oxygenated functional groups that are attached at the edge sites of GQDs. Firstly, the vibrational mode at $\sim$1000–1100 cm^{-1} is related to the C–O stretching vibrations.[22] The bands at $\sim$1360 cm^{-1} and $\sim$1580 cm^{-1} are attributed to the C–O epoxy deformation

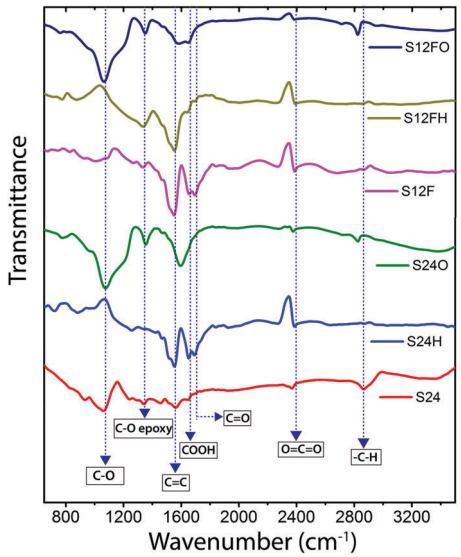

Fig. 8 FTIR transmittance spectra and associated vibrational modes of various pristine and annealed GQD samples showing the sp^2 carbon (C═C) and oxygenated edge functional groups (COOH, C═O/C–O).

and in-plane stretching vibrations of sp^2 hybridized carbon atoms (C═C), respectively.[21,50] Besides these, the edge functionalized oxygen functional groups can be clearly distinguished from the FTIR spectra (see Fig. 8). The vibrational modes at ~1650 and ~1700 cm^{-1} originate from the COOH and C═O edge functional groups.[22,50] Further, some weak bands at ~2366–2386 and ~2825 cm^{-1} are observed and are ascribed to the stretching vibrations of O═C═O and C–H modes, respectively.[45,50] Interestingly, the intensity of the C–O vibrational mode (1000–1100 cm^{-1}) is considerably increased for all O_2 annealed samples, suggesting the covalent attachment of oxygen atoms at the edge sites in GQDs. Note that this band nearly disappears after hydrogen annealing of S24, revealing the removal of some of the oxygen functional groups. However, other samples show the presence of this band even after H_2 annealing. Acik *et al.* suggested from the DFT simulation that the FITR vibrational bands at 1067, 1104, 1122, 1159, 1237 and 1296 cm^{-1} may originate from single or double vacancies of carbon atoms.[45] Thus, some of the FITR bands in the above region may be related to the defects in the hexagonal ring structure of GQDs. Note that our Raman analysis also suggested some crystal defects (vacancy and SW) in the GQD samples. On the other hand, the intensity of in-plane stretching vibrations of the C═C bond is relatively enhanced after annealing in both the environments (O_2 and H_2). This may be due to the high temperature (620 °C) annealing that leads to improvement in the C═C bond. Note that the oxygenated GQD thin films show considerable C–O epoxy bonds at the basal plane, although GQDs possess a high ratio of edge to basal plane carbon atoms (see Fig. 8). All these results are consistent with the PL analysis and peak assignments.

4. Conclusions

In conclusion, the formation mechanism of quasi-circular shaped GQDs was investigated from the TEM imaging of the GQDs formed at different stages of hydrothermal reaction. Our results suggest that in-plane epoxy (C–O–C) functional groups attached at the defect sites of oxidized graphene oxide (OGO) act as an active channel for the cutting of OGO into GQDs, as corroborated by UV-Vis absorption, TGA and FTIR analyses. This was corroborated by the absence of GQD formation when rGO was used as the precursor for the hydrothermal reaction. Further, using Raman and PL analyses, we probed the edge state conversion in GQD thin films before and after annealing at 620 °C under a controlled gas environment, for the first time. The blue PL emissions at ~407 and ~440 nm are unambiguously assigned to the zigzag and armchair free edge states in GQDs, while the two green PL emissions peaked at ~490 and ~530 nm are attributed to the COOH/C–OH and C═O/C–O edge oxygenated functional groups attached to GQD edges, respectively. The Raman spectra of GQDs were carefully analysed by deconvoluting the spectra using Gaussian and Lorentzian peak fitting. In addition to the characteristic Raman modes of graphene, such as D, G and D′ bands, we observed two new Raman bands at ~1260 and ~1440 cm^{-1} and these are assigned to COOH/C–OH and C═O edge oxygenated functional groups in GQDs, respectively. The Raman results were corroborated by the PL peak assignments. The structural, optical and compositional characteristics of GQD thin films were extensively studied by UV-Vis absorption, XPS and FTIR spectroscopy to corroborate the PL and Raman assignments. Our results provide significant new insights into the controlled growth of GQDs with tunable size and the edge state engineering of GQDs with tunable luminescence properties for future biosensors, optoelectronic, energy and environmental applications. The proposed growth mechanism for GQDs may stimulate further studies on the simulation and experimental demonstration of the cutting of GO sheets into different shaped GQDs through solution chemistry.

Acknowledgements

We acknowledge Central Instruments Facility, IIT Guwahati for providing the Raman and HRTEM facilities. Financial support from DEITY (Grant No. 5(9)/2012-NANO(VOL-II)) is acknowledged. We thank Dr K. Imakita, Kobe University, for the XPS measurement and Dr Ravi K. Biroju for help in some experiments.

References

1 A. K. Geim and K. S. Novoselov, *Nat. Mater.*, 2007, **6**, 183–191.
2 G. Eda and M. Chhowalla, *Adv. Mater.*, 2010, **22**, 2392–2415.
3 C. Gómez-Navarro, R. T. Weitz, A. M. Bittner, M. Scolari, A. Mews, M. Burghard and K. Kern, *Nano Lett.*, 2007, **7**, 3499–3503.
4 C. Gómez-Navarro, J. C. Meyer, R. S. Sundaram, A. Chuvilin, S. Kurasch, M. Burghard, K. Kern and U. Kaiser, *Nano Lett.*, 2010, **10**, 1144–1148.
5 S. H. Dave, C. Gong, A. W. Robertson, J. H. Warner and J. C. Grossman, *ACS Nano*, 2016, **10**, 7515–7522.

6 K. A. Ritter and J. W. Lyding, *Nat. Mater.*, 2009, **8**, 235–242.
7 L. R. Radovic and B. Bockrath, *J. Am. Chem. Soc.*, 2005, **127**, 5917–5927.
8 K. Lingam, R. Podila, H. Qian, S. Serkiz and A. M. Rao, *Adv. Funct. Mater.*, 2013, **23**, 5062–5065.
9 M. A. Montes-Morán, D. Suárez, J. A. Menéndez and E. Fuente, *Carbon*, 2004, **42**, 1219–1225.
10 L. A. Ponomarenko, F. Schedin, M. I. Katsnelson, R. Yang, E. W. Hill, K. S. Novoselov and A. K. Geim, *Science*, 2008, **320**, 356–358.
11 L. R. Radovic, *J. Am. Chem. Soc.*, 2009, **131**, 17166–17175.
12 C. Hyun, J. Yun, W. J. Cho, C. W. Myung, J. Park, G. Lee, Z. Lee, K. Kim and K. S. Kim, *ACS Nano*, 2015, **9**, 4669–4674.
13 Y. Kobayashi, K.-i. Fukui, T. Enoki, K. Kusakabe and Y. Kaburagi, *Phys. Rev. B: Condens. Matter Mater. Phys.*, 2005, **71**, 193406.
14 Z. Liu, Y. C. Lin, C. C. Lu, C. H. Yeh, P. W. Chiu, S. Iijima and K. Suenaga, *Nat. Commun.*, 2014, **5**, 4055.
15 J. Shen, Y. Zhu, X. Yang and C. Li, *Chem. Commun.*, 2012, **48**, 3686–3699.
16 Z. Zhang, J. Zhang, N. Chen and L. Qu, *Energy Environ. Sci.*, 2012, **5**, 8869–8890.
17 Z. Wang, H. Zeng and L. Sun, *J. Mater. Chem. C*, 2015, **3**, 1157–1165.
18 V. Gupta, N. Chaudhary, R. Srivastava, G. D. Sharma, R. Bhardwaj and S. Chand, *J. Am. Chem. Soc.*, 2011, **133**, 9960–9963.
19 S. Zhu, J. Zhang, X. Liu, B. Li, X. Wang, S. Tang, Q. Meng, Y. Li, C. Shi, R. Hu and B. Yang, *RSC Adv.*, 2012, **2**, 2717–2720.
20 D. Pan, J. Zhang, Z. Li and M. Wu, *Adv. Mater.*, 2010, **22**, 734–738.
21 Y. Sun, S. Wang, C. Li, P. Luo, L. Tao, Y. Wei and G. Shi, *Phys. Chem. Chem. Phys.*, 2013, **15**, 9907–9913.
22 J. Peng, W. Gao, B. K. Gupta, Z. Liu, R. Romero-Aburto, L. Ge, L. Song, L. B. Alemany, X. Zhan, G. Gao, S. A. Vithayathil, B. A. Kaipparettu, A. A. Marti, T. Hayashi, J.-J. Zhu and P. M. Ajayan, *Nano Lett.*, 2012, **12**, 844–849.
23 D. Qu, M. Zheng, L. Zhang, H. Zhao, Z. Xie, X. Jing, R. E. Haddad, H. Fan and Z. Sun, *Sci. Rep.*, 2014, **4**, 5294.
24 L. Tang, R. Ji, X. Cao, J. Lin, H. Jiang, X. Li, K. S. Teng, C. M. Luk, S. Zeng, J. Hao and S. P. Lau, *ACS Nano*, 2012, **6**, 5102–5110.
25 M. W. Lee, J. Kim and J. S. Suh, *RSC Adv.*, 2015, **5**, 67669–67675.
26 J. Kim and J. S. Suh, *ACS Nano*, 2014, **8**, 4190–4196.
27 J.-L. Li, K. N. Kudin, M. J. McAllister, R. K. Prud'homme, I. A. Aksay and R. Car, *Phys. Rev. Lett.*, 2006, **96**, 176101.
28 L. Wang, S.-J. Zhu, H.-Y. Wang, S.-N. Qu, Y.-L. Zhang, J.-H. Zhang, Q.-D. Chen, H.-L. Xu, W. Han, B. Yang and H.-B. Sun, *ACS Nano*, 2014, **8**, 2541–2547.
29 K. Habiba, V. I. Makarov, J. Avalos, M. J. F. Guinel, B. R. Weiner and G. Morell, *Carbon*, 2013, **64**, 341–350.
30 F. Liu, M.-H. Jang, H. D. Ha, J.-H. Kim, Y.-H. Cho and T. S. Seo, *Adv. Mater.*, 2013, **25**, 3657–3662.
31 S. Zhu, J. Zhang, S. Tang, C. Qiao, L. Wang, H. Wang, X. Liu, B. Li, Y. Li, W. Yu, X. Wang, H. Sun and B. Yang, *Adv. Funct. Mater.*, 2012, **22**, 4732–4740.
32 G. Sandeep Kumar, R. Roy, D. Sen, U. K. Ghorai, R. Thapa, N. Mazumder, S. Saha and K. K. Chattopadhyay, *Nanoscale*, 2014, **6**, 3384–3391.
33 J. Du, H. Wang, L. Wang, S. Zhu, Y. Song, B. Yang and H. Sun, *J. Mater. Chem. C*, 2016, **4**, 2235–2242.
34 H. Yoon, Y. H. Chang, S. H. Song, E.-S. Lee, S. H. Jin, C. Park, J. Lee, B. H. Kim, H. J. Kang, Y.-H. Kim and S. Jeon, *Adv. Mater.*, 2016, **28**, 5255–5261.
35 Y. Shin, J. Park, D. Hyun, J. Yang, J.-H. Lee, J.-H. Kim and H. Lee, *Nanoscale*, 2015, **7**, 5633–5637.
36 J. Chen, B. Yao, C. Li and G. Shi, *Carbon*, 2013, **64**, 225–229.
37 K. He, A. W. Robertson, Y. Fan, C. S. Allen, Y.-C. Lin, K. Suenaga, A. I. Kirkland and J. H. Warner, *ACS Nano*, 2015, **9**, 4786–4795.
38 N. R. Laine, F. J. Vastola and P. L. Walker, *J. Phys. Chem.*, 1963, **67**, 2030–2034.
39 T. Fan, W. Zeng, W. Tang, C. Yuan, S. Tong, K. Cai, Y. Liu, W. Huang, Y. Min and A. J. Epstein, *Nanoscale Res. Lett.*, 2015, **10**, 55.
40 G. Mercier, A. Klechikov, M. Hedenström, D. Johnels, I. A. Baburin, G. Seifert, R. Mysyk and A. V. Talyzin, *J. Phys. Chem. C*, 2015, **119**, 27179–27191.
41 R. Paola, H. Anming and C. Giuseppe, *Nano-Micro Lett.*, 2013, **5**, 260–273.
42 C. Su, M. Acik, K. Takai, J. Lu, S.-j. Hao, Y. Zheng, P. Wu, Q. Bao, T. Enoki, Y. J. Chabal and K. Ping Loh, *Nat. Commun.*, 2012, **3**, 1298.
43 A. Lerf, H. He, M. Forster and J. Klinowski, *J. Phys. Chem. B*, 1998, **102**, 4477–4482.
44 E. Fuente, J. A. Menéndez, M. A. Díez, D. Suárez and M. A. Montes-Morán, *J. Phys. Chem. B*, 2003, **107**, 6350–6359.
45 M. Acik, G. Lee, C. Mattevi, A. Pirkle, R. M. Wallace, M. Chhowalla, K. Cho and Y. Chabal, *J. Phys. Chem. C*, 2011, **115**, 19761–19781.
46 D. R. Dreyer, S. Park, C. W. Bielawski and R. S. Ruoff, *Chem. Soc. Rev.*, 2010, **39**, 228–240.
47 T. Sun and S. Fabris, *Nano Lett.*, 2012, **12**, 17–21.
48 Z. Li, W. Zhang, Y. Luo, J. Yang and J. G. Hou, *J. Am. Chem. Soc.*, 2009, **131**, 6320–6321.
49 D. V. Kosynkin, A. L. Higginbotham, A. Sinitskii, J. R. Lomeda, A. Dimiev, B. K. Price and J. M. Tour, *Nature*, 2009, **458**, 872–876.
50 R. K. Biroju, G. Rajender and P. K. Giri, *Carbon*, 2015, **95**, 228–238.
51 M. A. Sk, L. Huang, P. Chen and K. H. Lim, *J. Mater. Chem. C*, 2016, **4**, 6539–6545.
52 K. N. Kudin, B. Ozbas, H. C. Schniepp, R. K. Prud'homme, I. A. Aksay and R. Car, *Nano Lett.*, 2008, **8**, 36–41.
53 S. Claramunt, A. Varea, D. López-Díaz, M. M. Velázquez, A. Cornet and A. Cirera, *J. Phys. Chem. C*, 2015, **119**, 10123–10129.
54 A. Sadezky, H. Muckenhuber, H. Grothe, R. Niessner and U. Pöschl, *Carbon*, 2005, **43**, 1731–1742.
55 A. C. Ferrari and J. Robertson, *Phys. Rev. B: Condens. Matter Mater. Phys.*, 2000, **61**, 14095–14107.

56 S. L. H. Rebelo, A. Guedes, M. E. Szefczyk, A. M. Pereira, J. P. Araujo and C. Freire, *Phys. Chem. Chem. Phys.*, 2016, **18**, 12784–12796.
57 L. G. Cançado, M. A. Pimenta, B. R. A. Neves, M. S. S. Dantas and A. Jorio, *Phys. Rev. Lett.*, 2004, **93**, 247401.
58 C. Casiraghi, A. Hartschuh, H. Qian, S. Piscanec, C. Georgi, A. Fasoli, K. S. Novoselov, D. M. Basko and A. C. Ferrari, *Nano Lett.*, 2009, **9**, 1433–1441.
59 D. Bischoff, J. Güttinger, S. Dröscher, T. Ihn, K. Ensslin and C. Stampfer, *J. Appl. Phys.*, 2011, **109**, 073710.
60 Y. You, Z. Ni, T. Yu and Z. Shen, *Appl. Phys. Lett.*, 2008, **93**, 163112.
61 R. Nishinakagawa, K. Matsuda, T. Arai, A. Sawada and T. Terashima, *AIP Adv.*, 2013, **3**, 092111.
62 A. Ganguly, S. Sharma, P. Papakonstantinou and J. Hamilton, *J. Phys. Chem. C*, 2011, **115**, 17009–17019.
63 R. Balog, B. Jorgensen, L. Nilsson, M. Andersen, E. Rienks, M. Bianchi, M. Fanetti, E. Laegsgaard, A. Baraldi, S. Lizzit, Z. Sljivancanin, F. Besenbacher, B. Hammer, T. G. Pedersen, P. Hofmann and L. Hornekaer, *Nat. Mater.*, 2010, **9**, 315–319.
64 A. C. Ferrari and D. M. Basko, *Nat. Nanotechnol.*, 2013, **8**, 235–246.
65 B. Dippel, H. Jander and J. Heintzenberg, *Phys. Chem. Chem. Phys.*, 1999, **1**, 4707–4712.
66 Y. Li, H. Shu, S. Wang and J. Wang, *J. Phys. Chem. C*, 2015, **119**, 4983–4989.
67 M. Wimmer, A. R. Akhmerov and F. Guinea, *Phys. Rev. B: Condens. Matter Mater. Phys.*, 2010, **82**, 045409.
68 G. J. Soldano, M. F. Juarez, B. W. T. Teo and E. Santos, *Carbon*, 2014, **78**, 181–189.
69 B. Song, G. F. Schneider, Q. Xu, G. Pandraud, C. Dekker and H. Zandbergen, *Nano Lett.*, 2011, **11**, 2247–2250.

